



Cite this: *Soft Matter*, 2015, 11, 6294

From ribbons to tubules: a computational study of the polymorphism in aggregation of helical filaments†

Magdalena Gruzziel^{ab} and Piotr Szymczak^{*a}

A simple, coarse-grained model of chiral, helical filaments is used to study the polymorphism of fibrous aggregates. Three generic morphologies of the aggregates are observed: ribbons, in which the filaments are joined side-by-side, twisted, helicoidal fibrils, in which filaments entwine along each other and tubular forms, with filaments wound together around a hollow core of the tube. A relative simplicity of the model allows us to supplement numerical simulations with an analytic description of the elastic properties of the aggregates. The model is capable of predicting geometric and structural characteristics of the composite structures, as well as their relative stabilities. We also investigate in detail the transitions between different morphologies of the aggregates.

Received 19th March 2015,
 Accepted 15th June 2015

DOI: 10.1039/c5sm00652j

www.rsc.org/softmatter

1 Introduction

A number of biological macromolecules assemble in the form of fibre-like, typically helical forms. The examples include a wide variety of structures: from coiled-coils of α -helices, double-stranded DNA or protein fibrils, to microtubules and bacterial flagella. Even though these systems share a number of structural similarities, their detailed morphologies depend on the conformational characteristics at the monomeric level as well as the dynamics of the assembly process itself. For example, the fibrillogenesis depends on the type of fibrillized protein^{1–5} or the physical conditions during the fibrillization process,^{6,7} the DNA super-coil structure is influenced by the sequence of nucleotides, whereas the structure of a coiled-coil of α -helices changes depending on their amino acid sequences.⁸ Fibrillization processes have recently attracted a lot of attention, both due to their importance in the medical context and due to their potential application in bottom-up nanoengineering.⁹ On one hand, it has been realized that aggregation of proteins into amyloid fibrils is often associated with neurodegenerative diseases.¹⁰ On the other hand, many examples of functional fibrillar aggregates exist, the most famous of which are keratin, collagen, elastin, and silk with their unique elastic and tensile properties.¹¹ These structures have provided inspiration for nanoengineers for bottom-up

synthesis strategies, in which a small number of simple precursor molecules spontaneously assemble into hierarchical nanofibrils.¹² One of the basic questions in this context is how does the morphology of the fibrous superstructure depend on the properties of individual units and the dynamics of the aggregation process itself. Interestingly, despite a wide variety of building blocks, the set of realizable fibrillar superstructures seems to be relatively small. These include ribbons, in which the individual filaments are joined side-by-side, twisted, helicoidal structures in which several filaments are entwined along each other and tubular forms, with the filaments wound together around a hollow core of the tube.^{7,9,13–21}

Several models have been proposed to explain such a polymorphism, linking it to the action of hydrophobic, electrostatic or entropic forces.^{9,22} In particular, Adamcik *et al.*¹⁷ and Assenza *et al.*²³ have proposed models in which a key role in controlling the morphology of the aggregates is played by the competition between the electrostatic and elastic contributions to the total energy. While the electrostatic repulsion between like charges on different filaments is causing them to twist helically, the elastic energy prevents this twist from being excessive. Importantly, the helicity of the aggregates in this model is a consequence of the interactions between the individual filaments, which in itself are achiral.

Other researchers have invoked the role of chiralities of the constituent units. Chiral molecules do not pack parallel to their neighbors, but rather at a slight angle. Based on that observation, Aggeli *et al.*,¹⁴ Nyrkova *et al.*²⁴ and Selinger *et al.*²² have analyzed the properties of membranes formed by such chiral objects (which is reflected in the chiral elastic term in their Hamiltonian). Similarly to the studies based on electrostatic

^a Institute of Theoretical Physics, Faculty of Physics, University of Warsaw, Pasteura 5, 02-093, Warsaw, Poland. E-mail: Piotr.Szymczak@fuw.edu.pl

^b Interdisciplinary Centre for Mathematical and Computational Modeling, University of Warsaw, Pawińskiego 5a, 02-816, Warsaw, Poland

† Electronic supplementary information (ESI) available. See DOI: 10.1039/c5sm00652j

approaches, they also find that filaments self-assemble into helical or twisted ribbons, which can close on themselves forming the tubules.

However, as stated above, the starting point of the chirality models is a membrane Hamiltonian, thus they are better suited to describe self-assembly and polymorphism in lipids,^{25,26} colloidal membranes,²⁷ bilayers of gemini surfactants¹³ or amphiphiles,²⁸ but less suitable for description of the fibrillar aggregates. There is thus a gap in the literature which we attempt to fill in the present paper, by presenting the coarse-grained model of self-assembling chiral filaments, where we assume a microscopic Hamiltonian of each filament plus the interactions between them. A direct inspiration for our model is the molecular architecture of insulin aggregates. Insulin protofilaments are known to be helical,^{29,30} with a spine composed of steric zipper of β -strands, and the floppy C-termini of insulin chain B on the opposite sides of the filament winding around the filament axis. Because these termini are both hydrophobic and capable of association into interchain molecular velcro they tend to be attractive.³¹ This is reflected in our coarse grained model, where the filament backbone is represented by a chain of beads, whereas the second type of beads is used to represent the attractive interaction sites, arranged in two strips on the opposite sides of the backbone, each helically wound along the length of the filaments – arguably the simplest way of introducing chirality on the level of individual filaments. Thus the model falls into a similar class to those proposed by Aggeli *et al.* and Nyrkova *et al.*^{14,24} in that individual filaments are endowed with nonzero chirality. However, as already mentioned, we work on a finer scale than the models considered in ref. 24 and 14, resolving the energies and structure of individual filaments, instead of starting at the level of the multi-filament tapes, as it is the case therein.^{14,24}

Within this model, we analyze the structural forms attained by multi-filament clusters and the interconversions between them. Since the coarse-grained model resolves, albeit in a simplified way, the structure of individual filaments, it can account for different ways, in which (discrete) sets of binding sites on each filament can bind each other.^{32–34} In our previous paper, we have shown that the presence of such a discrete set of binding sites leads to a rather intricate dynamics of aggregation, accompanied by chirality inversions. It is thus of interest to see how this discreteness affects the cluster morphologies and the characteristics of the transitions between them, which is the main motivation for the present study. Interestingly, we still find three general morphological forms which the aggregates can attain, but their geometry is subtly different from that found in the continuum-sheet theories. For example, the helicoids created from the chiral filaments are not simply helicoidally twisted ribbons, but rather filaments winding around each other while sharing a common interaction seam, with the pitch determined by the arrangement of the binding sites, analogously to “knobs-into-holes” packing in coiled coils, as described by Crick.^{8,35,36} Similarly, the tubular structures that we found are stabilized by a set of discrete contacts between the individual filaments, which organize themselves

in a specific manner, giving rise to a selection of a well-defined radius of the tube.

Our aim here is to explore the energy landscape of the aggregating filaments for a given, fixed set of the parameters of the model, the same as the one used in our previous work on chirality reversals.³⁴ Within this framework, we identify the possible morphologies of the clusters, as well as look in detail at the transitions between the different morphological forms. Some of these transitions are found to be spontaneous, whereas to induce others one needs to apply force and/or increased temperature. We demonstrate that these morphologies, although described by a common set of parameters, arise as a result of an interplay between attraction of individual filaments and their elastic deformation energy, with individual terms responsible for bending, twisting and stretching of the filaments. Analysis of these energy contributions shows that their relative role changes depending on the superstructure of the cluster. A particularly important role is shown to be played by an anisotropy in bending rigidities, and the associated energy density, which gets massively released during the formation of the tubular structures. Importantly, a relative simplicity of the model allows us to supplement the numerical results with an analytic description of the filament aggregates, based on the continuum representation of the filaments in terms of the classical elasticity theory. This gives an additional insight into the energetics of the transition between different morphologies, enabling us to predict a range of parameters under which a given structure is expected to be stable. These predictions compare favorably with the numerical data. This paper is organized as follows. Section 2 presents the numerical model of aggregating filaments used in the present study. A continuum description of this model is introduced in Section 3. The core of the paper is the analysis of different aggregate morphologies and the transitions between them in Section 4. Finally, the conclusions are drawn in Section 5.

2 Coarse-grained model

The coarse-grained model of a filament used in this study is described in detail in ref. 22. Briefly, the filament backbone is represented by a chain of beads (gray beads in Fig. 1, marked with B), whereas a second type of beads is used to represent the attractive interaction sites, arranged in two strips on the opposite sides of the backbone, each helically wound along the length of the filament (white beads marked with S1 and S2 for each of strip, respectively). For the sake of brevity, we shall refer to these strips as “side-strands”.

In terms of bonding interactions, the force field includes harmonic potentials for both bonds (between consecutive B beads and between B bead and the adjacent S bead) and bond angles (between three consecutive B beads and between two consecutive B beads and one of the adjacent S beads). The equilibrium distance between the backbone beads, l^{BB} , is taken to be the length unit, whereas that between B bead and the adjacent S bead is $l^{BS} = 2l^{BB}$. The equilibrium bond angles correspond to the straight backbone (BBB angles equal to π)

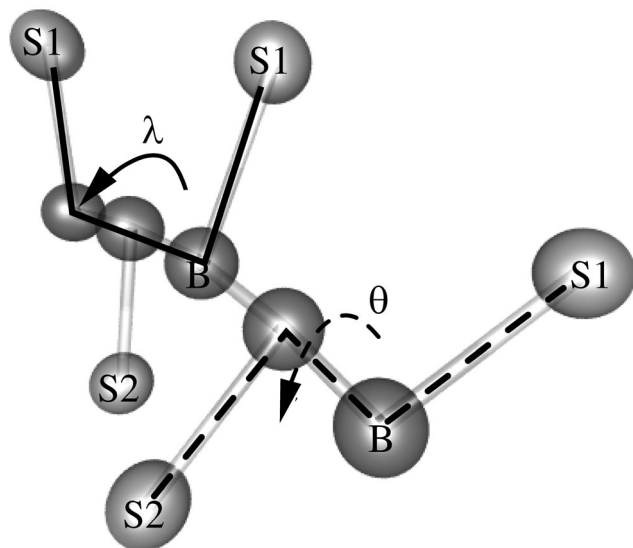


Fig. 1 Schematic of the model, with backbone beads in gray and side strand beads – white. Bonds defining the dihedral angles θ and λ are dashed and solid, respectively.

with perpendicular BS bonds (BBS angles equal to $\pi/2$). The key element of the model is the introduction of a symmetric double well dihedral potential U_θ associated with the dihedral angle spanned by four consecutive beads S1–B_r–B_{r+1}–S2 and denoted as θ in Fig. 1. The potential has two minima at $\theta = \pm\theta_0$ inducing local twist of the side strands, but also allowing for a flip of local chirality. The curvature of U_θ potential at the minima is characterized by the constant k_θ . Additionally, another dihedral potential, U_λ , is introduced, associated with the circumferential angle between a side strand bead and its neighbor (Fig. 1). The potential has the minima at $\pm\lambda_0 = \pm 2(\pi - \theta_0)$ and a barrier at $\lambda = 0$ with a barrier height $\Delta U_\lambda = U(0) - U(\pm\lambda_0) = k_\lambda/2\lambda_0^2$. The goal of this potential is to induce correlation between the values of the consecutive dihedrals and thus appearance of the overall twist of the side strands, with the twist density $\hat{\tau}_0 = \lambda_0/2l^{BB}$. The cohesive interactions between the filaments are mediated through the Lennard-Jones forces, $U_{LJ} = 4\epsilon \left[\left(\frac{\sigma}{r}\right)^{12} - \left(\frac{\sigma}{r}\right)^6 \right]$.

We use the uniform energy scale for backbone and side strand beads $\epsilon_B = \epsilon_S = \epsilon$ but different length scales: $\sigma_B = 4$ and $\sigma_S = 1$ (in the units of l^{BB}). The Lorentz–Berthelot combining rules are used to calculate the cross-species interaction parameters. The LJ energy is used as the energy and temperature unit throughout the paper, with the reduced temperature given by $T^* = k_B T/\epsilon$. All the filaments are composed of a fixed number of backbone and side strand beads, $n_B = 2n_{S1} = 2n_{S2} = 60$. The trajectories of the filaments are calculated using Langevin dynamics. A natural time scale in the simulations is set by the time it takes for a single bead to diffuse over the distance σ_B , i.e. $t_D = \frac{\gamma\sigma_B^2}{6k_B T}$, where γ is a single bead friction coefficient.

This time scale is used as a time unit in the data reported. The simulations were performed using the LAMMPS³⁷ molecular dynamics package.

3 Continuum description

Different morphologies of the filament clusters observed during the simulations of the aggregation process are shown in Fig. 2. Their appearance can be rationalized by noting that the driving force for the aggregation is the interaction between the helical side strands of each filament. When two such filaments are brought together then, for high enough binding energy between the beads, the side strands align forming an interaction seam, as indeed observed in Fig. 2b–d. The alignment of the side strands requires a certain amount of bending and twisting of the filaments. The interplay between bending, torsional and cohesive energies leads to the appearance of the local minima in the energy landscape. One of them corresponds to a situation when the filaments untwist to keep their backbones straight, forming planar, ribbon structures represented schematically in Fig. 2c.

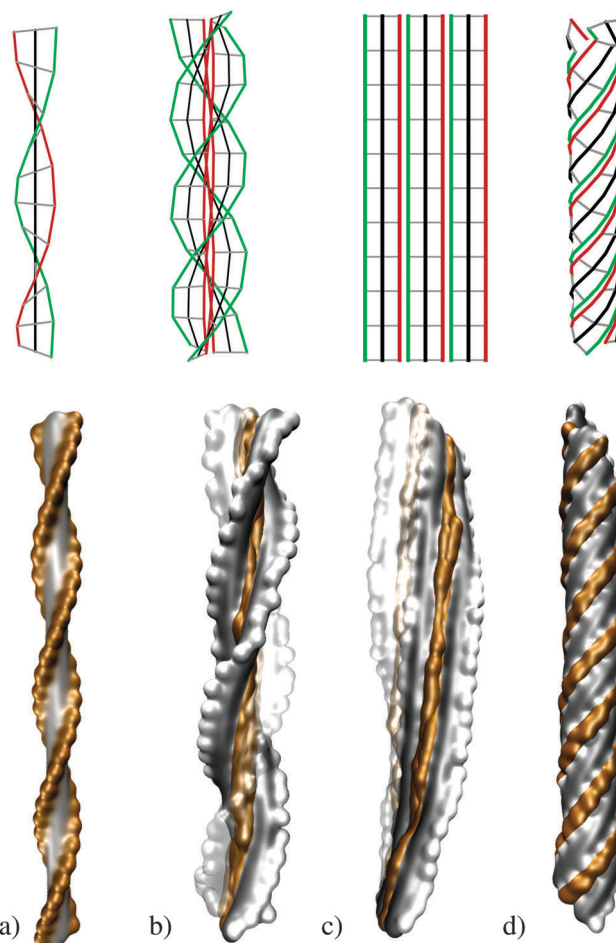


Fig. 2 Types of structures observed in the simulation of filament aggregation (bottom) and the schematic view of the corresponding binding modes between the filaments (top): (a) a single filament with two side strands marked in green and red respectively; (b) three filaments connected via the contacts between their side strands (red), making a helicoidal aggregate (c) untwisted filaments with straight side strands, forming a ribbon; (d) tubular shaft of helically wound filaments, forming a 'tubule' structure. In the bottom panels, the individual filaments are represented by the surface, with gray color marking backbones and brown marking contacting side strands. Bottom images created with VMD.³⁸

In such a case, the bending and cohesive energies are at their minimum, whereas the torsional energy is increased. Such a ribbon can close on itself, forming a tubular structure (Fig. 2d), with an additional stabilization due to the larger number of contacts between the filaments.

In the opposite case, when the twisting energy is at the minimum at the cost of increased bending energy, the filaments will tend to intertwine with each other forming helicoidal coiled coils, as depicted in Fig. 2b. As shown below, they can be transformed into the tubular structures by twisting.

To put these considerations on a more quantitative footing, let us consider the space curve $\mathbf{r}(s)$, tracing the axis of the filament, with s being the arc length. At each s , one can define the material frame built from the vector tangent to the filament axis (\vec{e}_3), the vector pointing towards the binding site (\vec{e}_1) and finally $\vec{e}_2 = \vec{e}_3 \times \vec{e}_1$. This basis evolves according to ref. 39

$$\frac{d\vec{e}_i}{ds} = (\hat{\tau}_0 \vec{e}_3 + \vec{Q}) \times \vec{e}_i \quad (1)$$

where \vec{Q} is a strain vector and $\hat{\tau}_0$ is the intrinsic twist density of the filament (side-strand twist angle around backbone per unit axial length). The energy associated with the elastic deformation of the backbone of the filament can then be expressed as

$$E_{\text{el}} = \frac{1}{2} \int_0^L (A_1 \Omega_1^2 + A_2 \Omega_2^2 + C \Omega_3^2) ds \quad (2)$$

where A_1 and A_2 are the bending stiffness coefficients and C is the torsional rigidity of the filament. Usually, it is more useful to express the above by means of the geometric characteristics of the filament axis: its curvature $\kappa(s)$, torsion $\tau(s)$ and the angle, $\zeta(s)$, between \vec{e}_2 and the Frenet–Serret normal, $\mathbf{n} = \frac{d\vec{e}_1}{ds}$.

In such a case,³⁹ $\Omega_1 = \kappa \sin \zeta$, $\Omega_2 = \kappa \cos \zeta$, thus the energy can be written as

$$E_{\text{el}} = \frac{1}{2} \int_0^L \left[(A_1 \kappa^2(s) + A_{\text{sp}} \kappa^2(s) \cos^2(\zeta) + C(\tau(s) - \hat{\tau}_0)^2) \right] ds \quad (3)$$

where $A_{\text{sp}} = A_2 - A_1$ measures the asymmetry of bending rigidities. The second term in the above expression gives the extra energy which is associated with bending along one axis in comparison to the other. It is sometimes called the splay elastic energy, particularly often encountered in the liquid crystals, where it is associated with the distortion mode characterized by a nonzero divergence of a director field.⁴⁰ In the context of elastic rods and ribbons splay becomes important whenever – due to anisotropy of the internal structure of a rod – it becomes more easy to bend it in a particular direction.^{24,41} In our case the anisotropy is associated with the presence of the side strand along the filament axis. Comparing the backbone with the side strand to a comb, one can intuitively see that bending in the plane of the teeth introduces an extra strain between the teeth, while bending in the perpendicular direction does not (teeth remain perpendicular to the backbone though the backbone itself gets bent, see Fig. 3). The exact relation between the effective parameters A_1 , A_2 and C and the coefficients

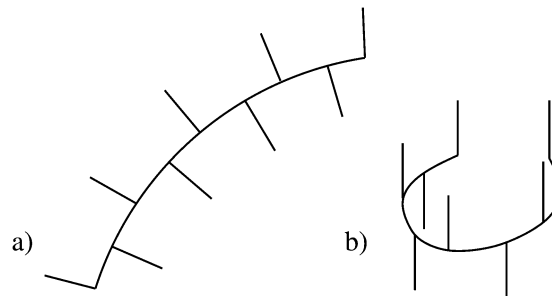


Fig. 3 Two bending modes of a comb: involving splay strain (a) and not involving it (b).

characterizing the coarse-grained model are discussed in Sections. S5 and S6 in the ESI.†

4 Aggregate morphologies and binding modes

4.1 Ribbons

When the filaments are put in solution, they begin to aggregate into clusters. If the internal twist of the filaments is relatively small ($\lambda_0 < 28^\circ$) then the first structures which appear during the aggregation usually are the ribbon forms of Fig. 2c. In these ribbons, the filaments are ordered side by side, with side strands untwisted to allow for a maximum number of contacts between the beads. However, such a geometric arrangement of the filaments is not energetically favorable, since each contact site binds two filaments only. This leads eventually to reorganization of the filaments into a more packed structure, in which they entwine one around the other to form helically twisted fibers (Fig. 2b). Notably, analogous ribbon structures have been observed in a number of experiments on aggregating proteins.^{6,7,15,18,20,21,42} Which of these shapes are realized is determined by the conditions of the aggregation (either quiescent or agitated^{6,15}) as well as pH.^{7,18} Clearly, the electrostatic environment around the growing fibril may have an impact on the protonation states of proteins and thus on the distribution of binding sites on the filament. On the other hand, even a slight change in the structure of the proteins may result in different elastic properties of the growing fibril. Interestingly, there are also cases in which ribbon and helicoidal forms coexist²⁰ and can be transformed into each other, in close analogy to what is observed in our simulations. Although for a particular parameter choice corresponding to the current model the ribbon structure is just a metastable intermediate form, by modifying the ratio between the bending and twisting rigidity and Lennard–Jones energy per contact (or the number of possible contacts), the ribbons can be made a kinetically favorable structure. This has been confirmed in ref. 20 where it has been shown that the mutations of human islet amyloid polypeptide destabilize the helical fibrils sufficiently relative to the ribbons and lead to their complete elimination.

4.2 Helicoids

Interestingly, the helicoidally twisted fibers themselves can exist in several conformational states. For small internal twists

of constituting filaments ($\hat{\tau}_0$) the filaments interact in a bead-by-bead manner: each S bead of one filament meets with its partner on the other (see Fig. 5a). This maximizes the number of bead-to-bead contacts, but comes at a cost of bending energy, since the filaments need to wind around each other. Eventually, for larger values of internal twist the cost in bending energy becomes too high and the cluster restructures itself into a configuration in which every n th side strand bead binds to a neighboring S bead on a second filament³⁴ (cf. Fig. 5b).

This reduces the twist of the filament backbone, since the effective twist density is now equal to

$$\hat{\tau}_n(\lambda_0) = \lambda_n/2nl^{\text{BB}}, \quad (4)$$

where

$$\lambda_n(\lambda_0) = -\pi + (n\lambda_0 + \pi) \bmod 2\pi \quad (5)$$

is the circumferential angle between a side strand bead and its n th neighbor wrapped to the interval $[-\pi, \pi]$. The optimal configuration of the cluster is then a result of a minimization of the total energy of the system, which (per unit contour length) is of the form

$$\frac{E_{\text{tot}}(\alpha)}{L} = A\kappa^2(\alpha) + A_{\text{sp}}\kappa^2(\alpha)\cos^2\xi + C(\tau(\alpha) - \hat{\tau}_n(\lambda_0))^2 + \frac{E_{\text{int}}}{L}, \quad (6)$$

where the curvature and torsion were reparametrized with superhelix helix angle α (that is the angle between the tangent to the helix and its axial line, Fig. 4) instead of arc length s and the cohesive interactions between the filaments, E_{int} , are approximated by the product of the contacts and the depth of the LJ potential well (see ESI† for a more detailed description). In principle, both the curvature and torsion are functions of the helix angle of the superhelix, α , and its radius, R (see Fig. 4):

$$\kappa = \frac{\sin^2 \alpha}{R}, \quad \tau = \frac{\sin \alpha \cos \alpha}{R}. \quad (7)$$

However, the radius of the superhelix is controlled by the strong binding interactions and is only weakly dependent on the specific binding mode. Hence, for a given binding mode (n) the energy of the system becomes the function of one variable only, α (see also ref. 32 for a similar approach). By minimizing eqn (6) with respect to α , *i.e.* finding α^* such that

$$\left(\frac{dE_{\text{tot}}}{d\alpha}\right)_{\alpha=\alpha^*} = 0, \quad (8)$$

we obtain the energies of binding modes as a function of the internal twist, λ_0 . Fig. 6 shows a plot of the optimal energy per unit length, $E_{\text{tot}}(\alpha^*)$, as obtained from eqn (6) for the first few binding modes. As observed up to $\lambda_0 \approx 48^\circ$ the most energetically favorable is $n = 1$ (bead-by-bead) mode, whereas for larger λ_0 the $n = 5$ mode becomes more favorable. The theoretical predictions are in very good agreement with the numerical simulations of the coarse-grained model of Section 2. Spontaneously formed clusters of the filaments bind in the $n = 1$ mode for $\lambda_0 < 40^\circ$ and in the $n = 5$ mode for $\lambda_0 > 48^\circ$ (intervals marked by arrows in Fig. 6). In the intermediate range of the

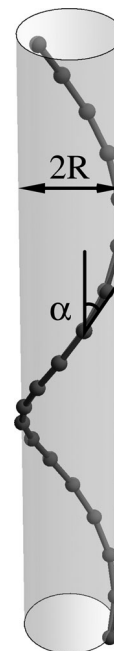


Fig. 4 Geometric parameters characterizing the supercoil: helix angle α and radius R .

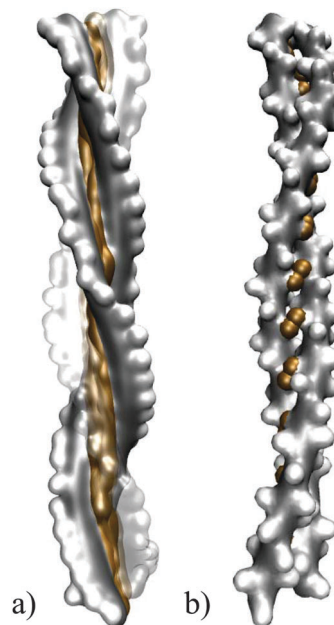


Fig. 5 Different binding modes in a helicoidal cluster: (a) $n = 1$ mode with the side strands binding in a bead-by-bead manner and (b) $n = 5$ mode in which every 5th side strand bead binds to a neighboring bead on a second filament (for clarity, only two filaments from a 3-filament cluster are shown here). The brown color marks the side strand beads in contact.

twist angles, the three energetically favorable modes, $n = 1$, $n = 5$, and $n = 7$, compete with each other, which results in inhomogeneous structures of mixed handedness. The bottom panel of Fig. 6 shows the value of the pitch of the optimum helical superstructures, $P = 2\pi R \cot \alpha^*$, compared with the average pitch measured in the simulations. An important phenomenon

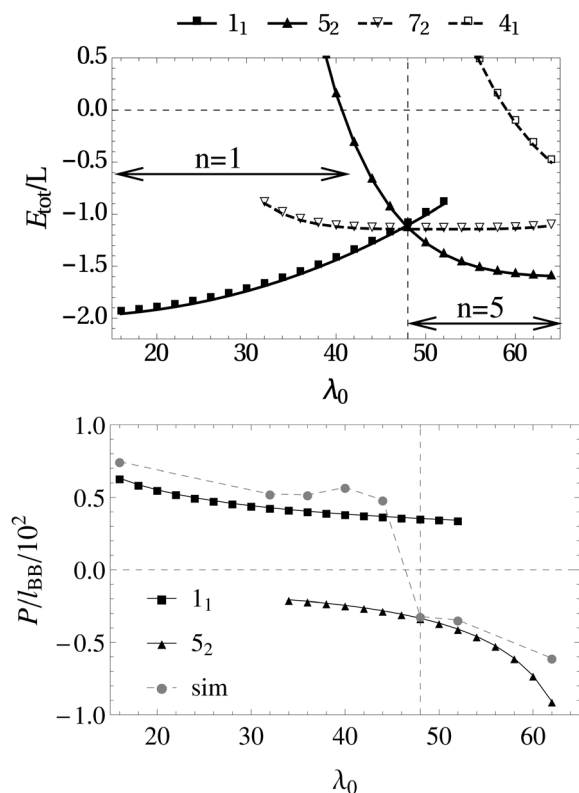


Fig. 6 Top: The theoretical predictions of the energies of the clusters in different binding modes obtained by minimization of the free energy, eqn (8). The modes correspond to a situation in which every n th side chain bead binds to a neighboring bead on another filament. The binding modes presented in the Figure correspond to $n = 1$ (filled squares), $n = 5$ (filled triangles), $n = 7$ (empty triangles) and $n = 4$ (empty squares). The lower indices (1, 2) mark the number of side strands involved in the formation of the interaction seam between the filaments. The arrows mark the intervals of λ_0 values in which a given mode is prevailing in the simulations. Bottom: the theoretical prediction of the pitch of the helicoidal superstructures calculated based on eqn (8) for the modes $n = 1$ and $n = 5$, compared with the simulation data.

observed here is the chirality inversion: the modes $n = 1$ and $n = 5$ are characterized by a different handedness (as determined by the sign of α^*) – supercoil of $n = 1$ mode maintains the same handedness as the individual filaments, whereas that for $n = 5$ – handedness opposite to that of individual strands. Interestingly, recent experiments by Usov *et al.*²¹ seem to confirm the existence of such a chirality-reversal transition in the fibrillization processes in bovine serum albumin.

4.3 Tubular structures

The aggregates can exist in yet another state, in which they form a tube of helically wound filaments ('tubular' structures of Fig. 2d). In the simulations, these structures are not observed to form spontaneously, because of the high free energy barrier between the helicoidal and tubular state, associated with the large amount of backbone bending needed to induce the transition. It is, however, possible to force the transition by twisting the helicoidal supercoil, much like what one would do while curling the macroscopic ribbons, as presented in Fig. 7.



Fig. 7 Analogy of ribbon, helicoidal and tubular states for a measuring tape. Grabbing the tape (a) by the ends and twisting it slightly, we put it into a helicoidal conformation (b). A somewhat larger twist induces a transition into the helical state (c). The difference between (b) and (c) lies in that in (b) the center line of the ribbon is straight and coincides with its symmetry axis, whereas in (c) the center line is a helix itself.

To be more precise, we clamp one end of the helicoidal supercoiled structure, while steadily ramping up the torque acting on the other end, $\mathcal{T} = at$ with torque rate $a \approx 0.1\epsilon/t_D$ up to $\mathcal{T}_{\text{max}} = 60\text{--}75\epsilon$. During the ramping process the aggregate first transforms itself from an initial helicoidal structure into the 'overtwisted' form (middle structure in Fig. 8) with a pitch reduced by a factor of 2 to 3, depending on the initial twist of the filaments. At that point the system encounters an energy barrier and further twist is impeded. The barrier is too high for the conformational transitions to occur during the accessible simulation time scales, unless the temperature is increased beyond $T^* = 1$.

The resulting transition leads to a dramatic conformational change within the cluster, accompanied by an abrupt rotation of the side strands. As observed in Fig. 9, the main difference

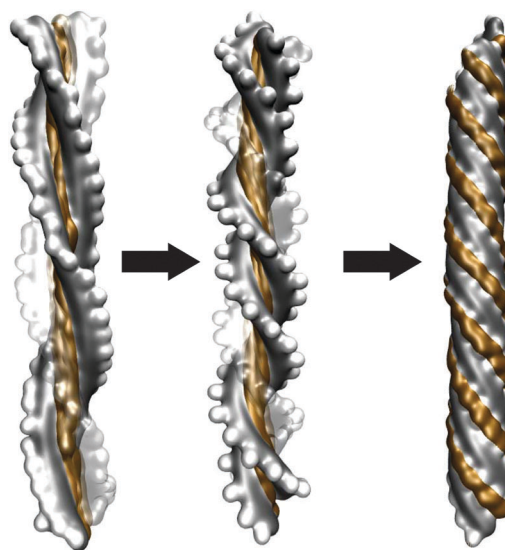


Fig. 8 Overtwisting of a helicoid leading to the formation of a tubular structure.

between the helicoidal and tubular structure is that in the former the side strands are turned towards the main axis (or outwards, depending on the side strand) whereas in the latter they are positioned along the surface of the tube. This can be quantified by an angle, ξ , between the backbone normal vector and side strand bond: it is close to zero in the overtwisted helicoidal conformation and $\pi/2$ in the tubular form.

A video illustrating the helicoid to tubule transition can be found in the ESI.† As can be seen from the video, the transition – although relatively abrupt – proceeds in a stepwise manner. As illustrated in more detail in Fig. 10, the transition starts locally, with a group of bonds in one of the filaments reorienting their side-strands from $\xi = 0$ to $\pi/2$. Then the transition “diffuses” towards the end of this filament (Fig. 10b). Once two filaments change their configuration, the whole structure becomes stabilized by the interacting side strands and then the last filament becomes locked in its place. The prominent role that the angle ξ plays in the helicoid–tubule transformation suggests that this transition can also be induced by applying the torque to one of the filaments in the overtwisted cluster, in order to increase the value of ξ within it (*cf.* Fig. 11). Except for being an efficient way of inducing the helicoid–tubule transition, such a controlled way of performing the transition provides insight into the energetics of the restructuring process. As presented in Fig. 12, the splay energy, accumulated during the overtwisting, is released during the transition to the tubular state. On the other hand, neither the torsional nor the backbone bending energy changes during the transition. Instead, they remain at their values acquired during the overtwisting, which are respectively smaller (for torsional) and larger (for bending energy) than the corresponding values for the unconstrained helicoid.

Importantly, there exists a range of intrinsic twist angles of the filaments ($\lambda_0 \in [18^\circ; 32^\circ]$) for which the tubular forms remain (meta)stable even after the torques are relaxed, with lifetimes of at least $4 \times 10^5 t_D$. These observations can be

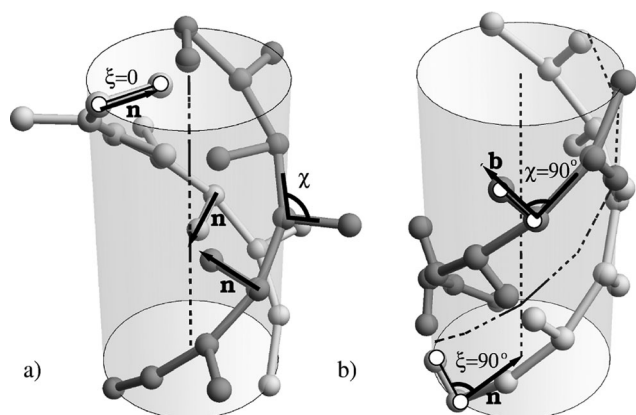


Fig. 9 Geometrical characteristics of the overtwisted (a) and tubular (b) structures (see also Fig. 8): χ – bond angles (S–B–B) of equilibrium value of $\pi/2$; ξ – the angle between the backbone normal vector and the side strand bond (it is roughly 0 in the overtwisted and twisted states and $\pi/2$ in the tubule). The strain in the χ angles is the source of an elastic splay term in the continuum description. See ESI† for details.

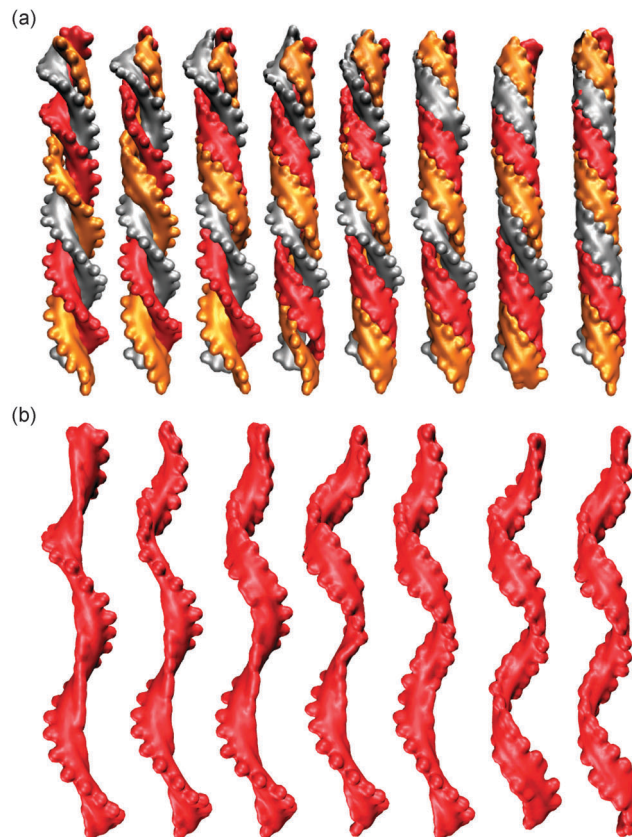


Fig. 10 (a) Example trajectory snapshots showing the transition from overtwisted (that is after the initial twisting phase, see text) helicoidal to tubular configuration. For clarity of presentation, (b) shows only a single filament. Images created using VMD.³⁸

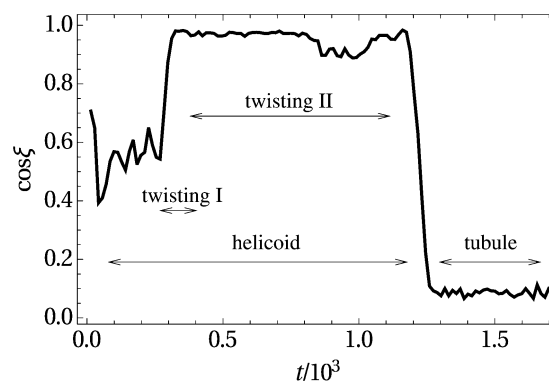


Fig. 11 Example time evolution of $|\cos \xi|$ (see Fig. 9) during the simulations with external torques applied at $T^* = 1.0$ and $\lambda_0 = 26^\circ$, where the twisting I phase is the initial stage with a constant torque rate applied to twist the helicoidal supercoil, and twisting II is the next stage with constant torques applied to single filaments.

rationalized in terms of a simplified, 1d energy landscape presented in Fig. 13. Here the solid line represents the situation in the absence of the torque. The helicoidal state (H) is then at the global energy minimum, separated by a wide and high barrier from the tubular form (T). As the torque is applied to the filament (phase 1 of the twisting), the landscape deforms

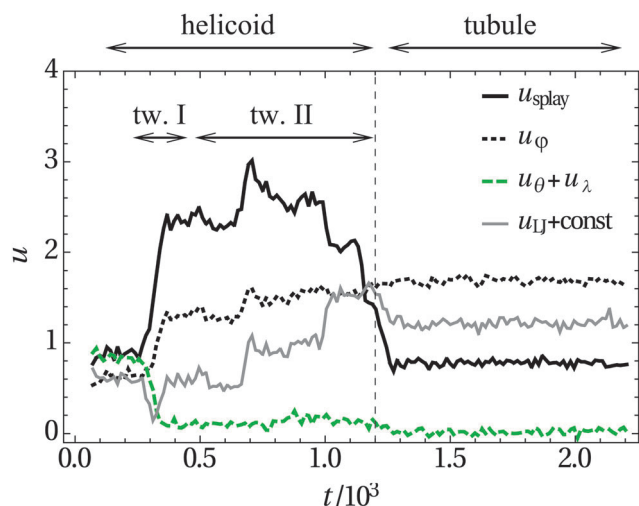


Fig. 12 Example time evolution of selected energy contributions during the simulations with external torques applied at $T^* = 1.0$ and $\lambda_0 = 26^\circ$ (twisting phases as in Fig. 11).

(dashed line in Fig. 13), and the cluster attains an overtwisted state (H^*). The remaining barrier between H^* and T can be overcome either stochastically or by additional twisting of one of the filaments (phase 2 of the twisting). This transition is marked by a dashed arrow in Fig. 13. After the torque is released, the tubular state remains at the local minimum. The energy barrier can be crossed stochastically (solid arrow in Fig. 13) which is accompanied by an abrupt release of the backbone strain with a simultaneous increase of dihedral and splay energy as the system goes back to the helicoidal form (Fig. 14). The change in splay energy is here relatively small, in contrast to the $H \rightarrow H^* \rightarrow T$ transition, where there is a large amount of splay strain involved in the overtwisted H^* structure.

The video illustrating the $T \rightarrow H$ transition can be found in the ESL.[†] The transition is slower than in the $H \rightarrow T$ case, but also takes place in a stepwise manner – it is initiated by loosening of

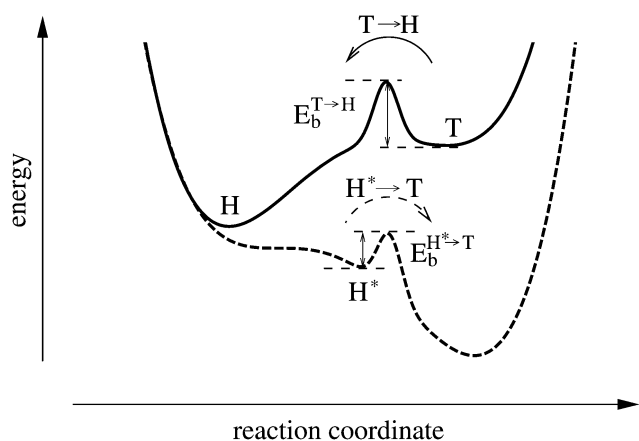


Fig. 13 Schematic of the energy landscape for helico-tubule transition. The helicoidal, overtwisted, and tubular conformations are denoted by H, H^* and T respectively. The dashed/solid line corresponds to the case with/without the external torque applied to the ends of the filament.

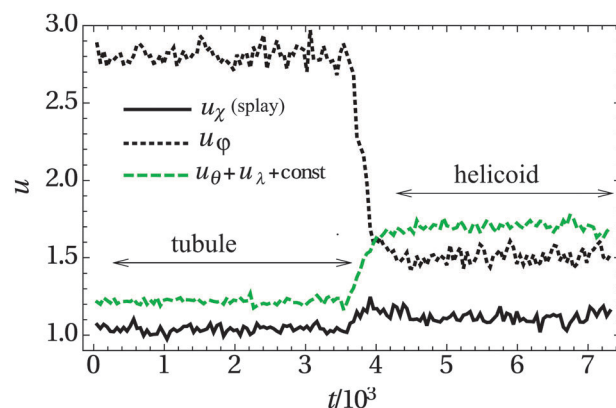


Fig. 14 The time evolution of the backbone bond angle, dihedral, and splay energies during $T \rightarrow H$ transition at $T^* = 1.3$ and $\lambda_0 = 26^\circ$.

the contacts between the filaments at their ends and then advancing towards the center of the aggregate.

To estimate the heights of the $H^* \rightarrow T$ and $T \rightarrow H$ energy barriers the rates of interconversion between these conformers were measured by performing a series of simulations at elevated temperatures and fitting them to the Arrhenius equation.^{43,44} The results, plotted as a function of λ_0 , are shown in Fig. 15. Note that the barrier heights depend on the maximum torque, \mathcal{F}_{\max} , used to overtwist the helicoid in phase 1 of the twisting – the larger the torque, the smaller the barrier left to overcome. This can again be related to the energy landscape shown in Fig. 13, where the position of H^* minimum shifts to the right as the torque is increased. Another interesting issue is the existence of the peak of maximum energy barrier at $\lambda_0 = 26^\circ$ pointing to more stable tubular structures at this intrinsic twist. Indeed, for these structures large temperature (even $T^* = 1.5$) is necessary to disrupt the tubules.

More insight into the forces stabilizing the helicoidal and tubular structure can be gained by the analysis of individual

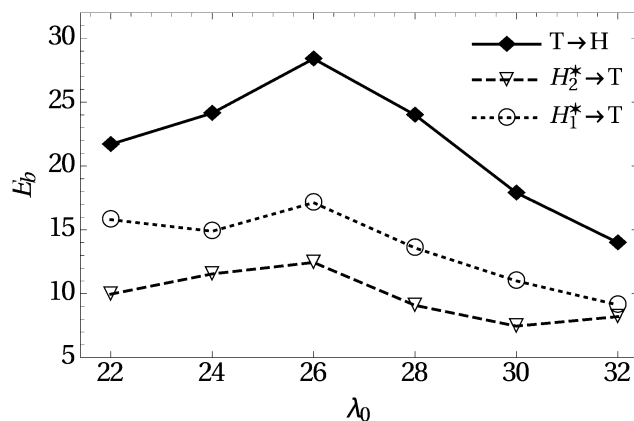


Fig. 15 The heights of energy barriers obtained from the simulation data for the tubule to helicoid ($T \rightarrow H$) transition (filled diamonds) and for the overtwisted helicoid to tubule ($H^* \rightarrow T$) transition (empty symbols). The overtwisted state H^* has been obtained with two different values of the maximum torque: H_1^* with $\mathcal{F}_1 = 62.5\varepsilon$ and H_2^* with $\mathcal{F}_2 = 75\varepsilon$. The lines are the guide to the eye.

contributions to the internal energy (Fig. S3a–d, ESI†). Although significantly different in shape, both the helicoidal and tubular conformations maintain a similar number and quality of contacts, that is the difference between the two structures in the cohesive energy is small (Fig. S3d, ESI†), particularly, relatively to other contributions. Also, the difference in the bond energy is negligible (Fig. S3a, ESI†). Clearly, the two competing forces in the cylindrical structure is the one aiming at straightening the backbone (towards the helicoidal configuration, with the backbone only slightly bent) competing with the one aiming at keeping the torsion of the backbone helix at $\tau = \hat{\tau}_0$ which minimizes the dihedral term in the elastic energy, as given in eqn (6).

The tubular structures have a very robust geometry. They are formed by three filaments wound together around a hollow core of the tube. The LJ attraction forces between the backbone beads stabilize their distance at $d_0 = 2^{1/6} \sigma_B$. The cross-section of the tubule coincides then with a circle circumscribed on the equilateral triangle with a side length of d_0 (see Fig. 16). This sets the circle radius at $R = 4 \times 2^{1/6} \times 3^{-1/2} \approx 2.59$, where we have used the fact that $\sigma_B = 4$ (in the units of l^{BB}). This value of the radius is not far from the simulation results, where $\langle R \rangle \approx 2.65 \pm 0.1$ has been obtained. However, d_0 is also the distance between the filament backbones as measured along the side of the cylinder (cf. Fig. 16). By solving the triangle marked in the left panel of Fig. 16, we get $P = 6\pi R d_0 (4\pi^2 R^2 - 9d_0^2)^{-1/2} \approx 23.958$, which is very close to the average pitch of the tubular structures measured in the simulations ($\langle P \rangle = 23.3 \pm 0.4$). Finally, the helix angle of the tubule can be calculated to be $\alpha = 34.2^\circ$.

These values of R and α , together with A_1 , A_{sp} and C parameters given in the ESI† can then be used in eqn (6) to estimate the free energy of tubular structures, as shown in Fig. 17. Also, the energies of helicoids, overtwisted helicoids and ribbons are presented there. The ribbon energies are approximated by assuming straight configuration of the filaments, with the only strain coming from the untwisted side-strands. The ribbons and tubules are structurally similar to each other, with the main difference coming from the fact that the latter form a closed structure, with a larger number of contacts between the backbones

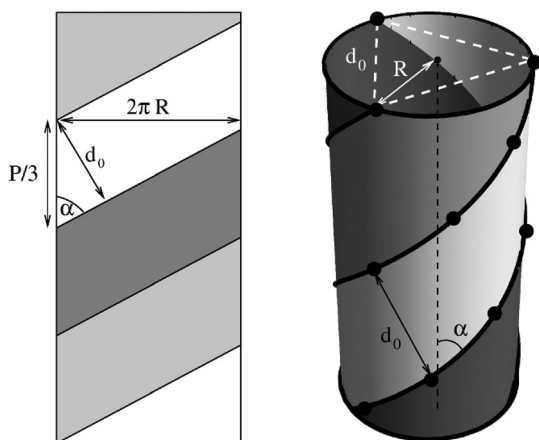


Fig. 16 Arrangements of the filaments within the tubule.

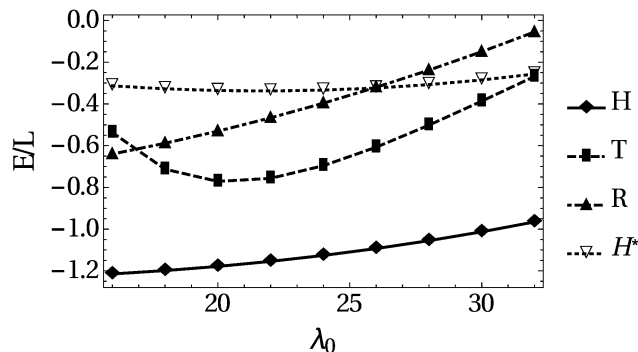


Fig. 17 Theoretical estimates of the free energy per unit length of the helicoid (filled diamonds), overtwisted helicoid (empty triangles), ribbon (filled triangles), and tubule (filled rectangles) systems at $T^* = 1.0$ for various values of intrinsic filament twist angle, λ_0 .

and the side strands, and hence lower LJ energy, stabilizing the structure. There are approximately 450 contacts in 3-filament cluster of a tubular form (180 B–B contacts, 90 S–S contacts and 180 S–B contacts), which gives on average 2.5 contacts per unit length of each filament. An analogous calculation for the ribbon gives a value of 1.67 contacts per unit length.

Finally, the energies of overtwisted helicoidal structures are calculated similarly to those of the tubules, based on the observation that neither the pitch nor the radius changes significantly during the $H^* \rightarrow T$ transition. This, together with the assumption that $\xi = 0$ fully determines the geometry of these structures.

It is worth noting a pronounced minimum in the tubule energy plot (cf. Fig. 17) at around $\lambda_0 = 20^\circ$. This is related to the dihedral term, $C(\tau - \hat{\tau}_0)^2$ in the energy eqn (6). The torsion of the tubule, calculated based on eqn (7), with $\alpha = 34.2^\circ$ reads $\tau \approx 0.179$. Since, on the other hand, $\hat{\tau}_0 = \lambda_0/2l^{BB}$, one concludes that for $\lambda = 0.358$ radians (or 20°) the dihedral term vanishes, hence the parabolic form of the energy plot in this region. This minimum, suggesting the increased stability of the tubules at $\lambda_0 = 19\text{--}21^\circ$, should be compared with the maximum in the barrier heights shown in Fig. 15 which marks the most stable tubules obtained in the simulations. However, the maximum is shifted to $\lambda_0 = 26^\circ$ which is probably the result of a simplified treatment of LJ interactions between side-strand beads in the analytic model. When calculating the interactions between the side strands in the tubule, we assume that they are directed along the backbone binormal vectors. However, at the same time the attractive interactions between the backbones try to bring the distance between them to the equilibrium value of d_0 . To accommodate that, the side strand beads have to slightly protrude out of the cylinder surface, which is the reason why the optimal angle in the real system shifts by approximately 10% with respect to that predicted by a theory.

Finally, let us note that there are in principle two ways in which the tubules can be formed. One is by twisting the helicoidal structures, as described above. The other possibility of tubule formation would be directly from the ribbon, which can wrap around and close on itself. However, in the present

model a large difference in energies between the ribbons and the helicoids creates a strong bias towards the latter. As a result, the ribbons are transient structures only and get transformed into the helicoids before they manage to form tubules.

5 Concluding remarks

In this paper, we have presented a simple model of aggregating helical filaments, capable of describing the transitions between different aggregate morphologies: ribbon-like, helicoidal, and tubular. A relative simplicity of the model allowed for an introduction of analytic description, based on a linear elastic model of helical filaments interacting through multiple binding sites. We studied the dependence of the results on the intrinsic twist of the filaments. The theoretical model predicts nicely the crossover between binding modes in the case of helicoidal clusters, as well as the existence of the most stable forms of the tubules. We have quantified the geometrical characteristics of different morphological types as well as the main energy contributions determining their relative stability. We conclude with two remarks. First, as already mentioned in the Introduction, there are both similarities and differences between the geometries of the aggregate structures in the present study and those based on the continuum sheet theories.^{13,14,22,45–48}

On one hand, the overall topological features, with the division into three main structural classes – ribbons, helicoids and tubules – are similar in both approaches. However, at a finer level of detail a number of differences are evident. The helicoids are not simply twisted ribbons, as in the continuum theories, but rather coiled coils composed of filaments winding around each other while sharing a common interaction seam. Similarly to the “knobs-into-holes” packing in α -helical coiled coils described by Crick and others,^{8,35,36} we find that the filaments forming a helicoid can bind themselves in a number of different ways (“binding modes”), the selection of which depends on the internal twist of the individual filaments. The binding modes determine both the pitch and the handedness of the resulting cluster. The network of contacts between the binding sites with an underlying triangular ordering (*cf.* Fig. 17) also provides a stabilizing scaffold for the tubular structure, giving rise to the selection of a well-defined radius of the tube.

Second, the numerical data and theoretical considerations presented here seem to suggest that it should be relatively easy to induce a transition between different morphological forms. The easiest way of carrying it out is to change the relative magnitude of cohesive and elastic contributions to the energy. This can be achieved by changing the ionic strength (which can screen the electrostatic interactions between the binding sites) or temperature. Importantly, these factors not only influence the interaction between the filaments but can also affect the properties of individual filaments, such as their internal twist (λ_0), which in turn influences the properties of the aggregate, including its handedness. An increased sensitivity of the aggregate characteristics to the environmental conditions has indeed been observed in many experimental studies.^{6,7,18,21,47} Such a

possibility of dynamic morphology control makes these materials particularly attractive from the point of view of bottom-up nanotechnology.

Acknowledgements

MG acknowledges support from the Foundation for Polish Science (FNP) through TEAM/2010-6/2 project co-financed by the EU European Regional Development Fund, and the PL-Grid Infrastructure (Grant ID: plgly, Hydra Supercomputer). PS acknowledges support from the National Science Centre (Grant No. N N202 055440). Helpful discussions with Marek Cieplak on the aggregation models are gratefully acknowledged.

References

- 1 J. L. Jiménez, E. J. Nettleton, M. Bouchard, C. V. Robinson, C. M. Dobson and H. R. Saibil, *Proc. Natl. Acad. Sci. U. S. A.*, 2002, **99**, 9196.
- 2 Y. Miller, B. Ma and R. Nussinov, *Chem. Rev.*, 2010, **110**, 4820–4838.
- 3 T. Lührs, C. Ritter, M. Adrian, D. Riek-Loher, B. Bohrmann, H. Döbeli, D. Schubert and R. Riek, *Proc. Natl. Acad. Sci. U. S. A.*, 2005, **102**, 17342–17347.
- 4 C. Sachse, C. Xu, K. Wieligmann, S. Diekmann, N. Grigorieff and M. Fändrich, *J. Mol. Biol.*, 2006, **362**, 347.
- 5 L. C. Serpell, M. Sunde, M. D. Benson, G. A. Tennent, M. B. Pepys and P. E. Fraser, *J. Mol. Biol.*, 2000, **300**, 1033.
- 6 A. Lokszejn and W. Dzwolak, *J. Mol. Biol.*, 2008, **379**, 9–16.
- 7 D. Kurouski, R. K. Dukor, X. Lu, L. A. Nafie and I. K. Lednev, *Biophys. J.*, 2012, **103**, 522–531.
- 8 A. N. Lupas and M. Gruber, in *Advances in Protein Chemistry, Fibrous Proteins: Coiled-Coils, Collagen and Elastomers*, ed. D. Parry and J. Squire, Elsevier, 2005, vol. 70, pp. 37–78.
- 9 J. Adamcik and R. Mezzenga, *Macromolecules*, 2012, **45**, 1137–1150.
- 10 A. Kajava, J. Squire and D. A. D. E. Parry, *Advances in Protein Chemistry, Fibrous Proteins: Amyloids, Prions and Beta Proteins*, Elsevier, Academic Press, 2006, vol. 73.
- 11 J. Squire and D. A. D. E. Parry, *Advances in Protein Chemistry, Fibrous Proteins: Muscle and Molecular Motors*, Elsevier, Academic Press, 2005, vol. 71.
- 12 T. Vo-Dinh, *Protein Nanotechnology - Protocols, Instrumentation, And Applications*, Humana Press, 1st edn, 2010.
- 13 R. Oda, I. Huc, M. Schmutz, S. J. Candau and F. C. MacKintosh, *Nature*, 1999, **399**, 566–569.
- 14 A. Aggeli, I. A. Nyrkova, M. Bell, R. Harding, L. Carrick, T. C. B. McLeish, A. N. Semenov and N. Boden, *Proc. Natl. Acad. Sci. U. S. A.*, 2001, **98**, 11857–11862.
- 15 A. T. Petkova, R. D. Leapman, Z. Guo, W.-M. Yau, M. P. Mattson and R. Tycko, *Science*, 2005, **307**, 262–265.
- 16 J. Adamcik, J.-M. Jung, J. Flakowski, P. De Los Rios, G. Dietler and R. Mezzenga, *Nat. Nanotechnol.*, 2010, **5**, 423–428.
- 17 J. Adamcik and R. Mezzenga, *Soft Matter*, 2011, **7**, 5437–5443.

- 18 D. Kurovski, X. Lu, L. Popova, W. Wan, M. Shanmugasundaram, G. Stubbs, R. K. Dukor, I. K. Lednev and L. A. Nafie, *J. Am. Chem. Soc.*, 2014, **136**, 2302–2312.
- 19 L. R. Volpatti, M. Vendruscolo, C. M. Dobson and T. P. Knowles, *ACS Nano*, 2013, **7**, 10443–10448.
- 20 S. Zhang, M. Andreassen, J. T. Nielsen, L. Liu, E. H. Nielsen, J. Song, G. Ji, F. Sung, T. Skrydstrup, F. Besenbacher, N. C. Nielsen, D. E. Otzen and M. Dong, *Proc. Natl. Acad. Sci. U. S. A.*, 2013, **110**, 2798–2803.
- 21 I. Usov, J. Adamcik and R. Mezzenga, *ACS Nano*, 2013, **7**, 10465–10474.
- 22 J. V. Selinger, M. S. Spector and J. M. Schnur, *J. Phys. Chem. B*, 2001, **105**, 7157–7169.
- 23 S. Assenza, J. Adamcik, R. Mezzenga and P. De Los Rios, *Phys. Rev. Lett.*, 2014, **113**, 268103.
- 24 I. A. Nyrkova, A. N. Semenov, A. Aggeli and N. Boden, *Eur. Phys. J. B*, 2000, **17**, 481–497.
- 25 D. S. Chung, G. B. Benedek, F. M. Konikoff and J. M. Donovan, *Proc. Natl. Acad. Sci. U. S. A.*, 1993, **90**, 11341–11345.
- 26 Y. V. Zastavker, N. Asherie, A. Lomakin, J. Pande, J. M. Donovan, J. M. Schnur and G. B. Benedek, *Proc. Natl. Acad. Sci. U. S. A.*, 1999, **96**, 7883–7887.
- 27 T. Gibaud, E. Barry, M. J. Zakhary, M. Henglin, A. Ward, Y. Yang, C. Berciu, R. Oldenbourg, M. F. Hagan and D. Nicastro, *et al.*, *Nature*, 2012, **481**, 348–351.
- 28 L. Ziserman, H.-Y. Lee, S. R. Raghavan, A. Mor and D. Danino, *J. Am. Chem. Soc.*, 2011, **133**, 2511–2517.
- 29 B. Vestergaard, M. Groenning, M. Roessle, J. S. Kastrup, M. Van De Weert, J. M. Flink, S. Frokjaer, M. Gajhede and D. I. Svergun, *PLoS Biol.*, 2007, **5**, e134.
- 30 M. I. Ivanova, S. A. Sievers, M. R. Sawaya, J. S. Wall and D. Eisenberg, *Proc. Natl. Acad. Sci. U. S. A.*, 2009, **106**, 18990–18995.
- 31 V. Babenko and W. Dzwolak, *FEBS Lett.*, 2013, **587**, 625–630.
- 32 S. Neukirch, A. Goriely and A. C. Hausrath, *Phys. Rev. Lett.*, 2008, **100**, 038105.
- 33 C. W. Wolgemuth and S. X. Sun, *Phys. Rev. Lett.*, 2006, **97**, 248101.
- 34 M. Gruzziel, W. Dzwolak and P. Szymczak, *Soft Matter*, 2013, **9**, 8005.
- 35 F. Crick, *Acta Crystallogr.*, 1953, **6**, 689–697.
- 36 G. Offer, M. R. Hicks and D. N. Woolfson, *J. Struct. Biol.*, 2002, **137**, 41–53.
- 37 S. Plimpton, *J. Comput. Phys.*, 1995, **117**, 1–19.
- 38 W. Humphrey, A. Dalke and K. Schulten, *J. Mol. Graphics*, 1996, **14**, 33–38.
- 39 J. F. Marko and E. D. Siggia, *Macromolecules*, 1994, **27**, 981–988.
- 40 H. Deuling, *Liquid Crystals, Solid State Physics*, 1978, **14**, 103–107.
- 41 J. B. Fournier, *Phys. Rev. Lett.*, 1996, **76**, 4436.
- 42 C. Lara, S. Handschin and R. Mezzenga, *Nanoscale*, 2013, **5**, 7197–7201.
- 43 M. Schlierf, H. Li and J. M. Fernandez, *Proc. Natl. Acad. Sci. U. S. A.*, 2004, **101**, 7299.
- 44 P. Szymczak and M. Cieplak, *J. Phys.: Condens. Matter*, 2006, **18**, L21.
- 45 R. L. B. Selinger, J. V. Selinger, A. P. Malanoski and J. M. Schnur, *Phys. Rev. Lett.*, 2004, **93**, 158103.
- 46 R. Ghafouri and R. Bruinsma, *Phys. Rev. Lett.*, 2005, **94**, 138101.
- 47 Y. Sawa, F. Ye, K. Urayama, T. Takigawa, V. Gimenez-Pinto, R. L. B. Selinger and J. V. Selinger, *Proc. Natl. Acad. Sci. U. S. A.*, 2011, **108**, 6364–6368.
- 48 L. Teresi and V. Varano, *Soft Matter*, 2013, **9**, 3081–3088.